

Emergent active turbulence and intermittency in dense algal suspensions of *Chlamydomonas reinhardtii*

Prince Vibek Baruah,^{1,*} Nadia Bihari Padhan,^{2,1,†} Biswajit Maji,^{1,‡} Rahul Pandit,^{1,§} and Prerna Sharma^{3,1,¶}

¹*Department of Physics, Indian Institute of Science, Bangalore 560012, India*

²*Institute of Scientific Computing, TU Dresden, 01069 Dresden, Germany*

³*Department of Bioengineering, Indian Institute of Science, Bangalore 560012, India*

(Dated: March 13, 2025)

Active-fluid turbulence has been found in bacterial suspensions, but not so far in their algal counterparts. We present the first experimental evidence for turbulence in dense algal suspensions of *Chlamydomonas reinhardtii*. We carry out a detailed analysis of the statistical properties of the flow present in these cell suspensions and show that they are quantitatively distinct from their counterparts in two-dimensional fluid and bacterial turbulence. Both kinetic-energy and density spectra of the fluid flow in algal turbulence show power-law regimes with unique scaling exponents. The fluid velocity probability distribution function (PDF) is strongly non-Gaussian and the length dependence of the PDF of fluid-velocity increments indicates small-scale intermittency. We compare and contrast our results with recent theoretical predictions for active-scalar turbulence and active glasses. Overall, our results highlight that active turbulence can arise, even in absence of orientational instabilities, so it is not limited to bacterial suspensions but it can also be found in many biological systems with free-swimming micro-organisms.

I. UNCOVERING ALGAL TURBULENCE

Turbulence, which is ubiquitous from astrophysical to cellular scales [1–7], continues to provide new and exciting challenges for physicists, engineers, and mathematicians. Nonequilibrium turbulence-like states, which have been found over the last decade or so in dense bacterial suspensions [8–14], provide important recent examples of new types of turbulence. This has been christened *active turbulence* because such suspensions are *active fluids* in which energy is injected into the fluid not by an external force, as in conventional fluid turbulence, but by the conversion of chemical sources of energy to kinetic energy by the constituents in the suspension [12].

Our work is inherently interdisciplinary because it studies complex flows in a biological system using techniques from turbulence theories and simulations. We present the first experimental study of emergent active turbulence and intermittency in *dense* algal systems. In particular, we carry out experiments on suspensions of two types of *Chlamydomonas reinhardtii* (henceforth, *C. reinhardtii*), the wild type (WT) and the mutant mbo2. We then characterise the statistical properties of this algal turbulence using measures that are employed to study conventional fluid turbulence. We compare our results with recent theoretical and numerical studies of scalar active turbulence [15].

We obtain kinetic-energy and algal-concentration spectra, longitudinal-velocity structure functions [1, 3–5,

16], probability distribution functions (PDFs) of velocity components, length-scale dependent longitudinal-velocity increments, and the Okubo-Weiss parameter Λ , which distinguishes between vortical and extensional regions in a flow. These spectra display power-law scaling regions as a function of the wavenumber k ; and they indicate that kinetic-energy and concentration fluctuations are spread over a wide range of spatial scales; these are clear signatures of turbulence. However, the power-law exponents that characterise these scaling regions are distinctly different from their fluid-turbulence and bacterial-turbulence counterparts [1, 3–5, 12], as are the PDFs and structure functions mentioned above. Thus, our investigations uncover a new type of active turbulence, which we call *algal turbulence*, and whose special statistical properties we elucidate below. Earlier experimental and theoretical studies [17–19] have investigated enhanced tracer diffusion in *dilute* suspensions of swimming eukaryotic swimmers like *C. reinhardtii*. However, this enhanced tracer diffusion is more akin to Lagrangian chaos or passive-scalar intermittency in simple flows [20–22] than to the fully developed algal turbulence we have uncovered here.

As we increase the concentration of *C. reinhardtii* cells, the temporal evolution of our dense algal suspensions slows down and the intensity of algal turbulence in our systems decreases. Therefore, it behooves us to explore whether our algal systems cross over from algal turbulence to an *active algal glass*. To examine this possibility for the cells in our suspensions, we calculate several quantities that are used to characterise slow dynamics in active glasses [23–25], including (a) the mean-square displacement (MSD), (b) the self-intermediate scattering function $F_s(k, t)$, (c) the overlap function $Q(t)$, and (d) the four-point correlation function $\chi_4(t)$, which characterises the dynamic heterogeneity in a glassy system. Our systems exhibit dynamic heterogeneity and distinct

* princebaruah@iisc.ac.in

† nadia.bihari.padhan@tu-dresden.de

‡ biswajitmaji@iisc.ac.in

§ rahul@iisc.ac.in

¶ prerna@iisc.ac.in

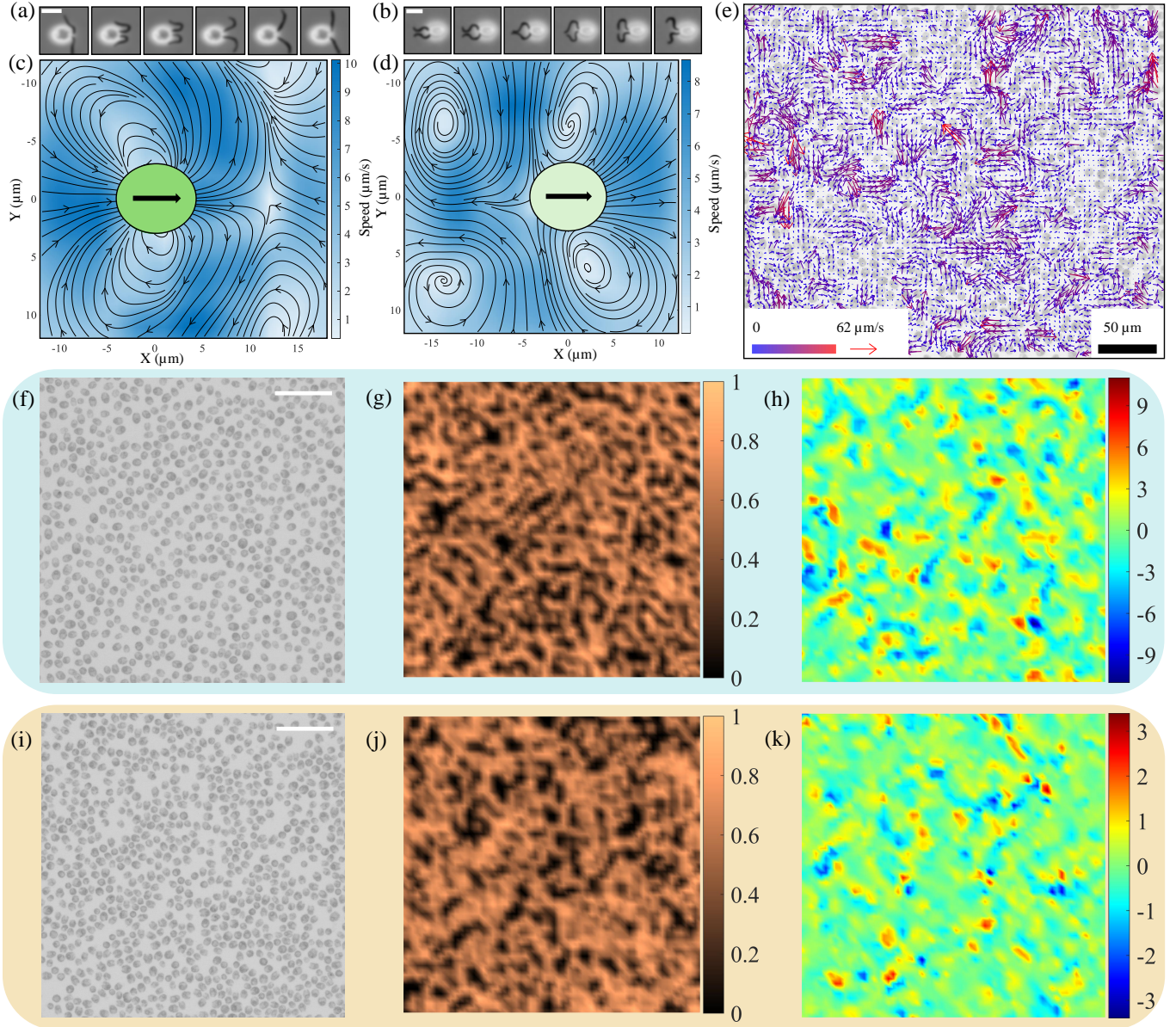


FIG. 1. Time-lapse images of the motion of an isolated (a) wild-type (WT) and (b) *mbo2* *C. reinhardtii* cell [scale bar, 10 microns]. Experimentally measured beat averaged flow-fields of isolated (c) WT and (d) *mbo2* *C. reinhardtii* cells; the arrow indicates the direction of motion. (e) Velocity-vectors, obtained from particle-image velocimetry (PIV), overlaid on the image of a dense suspension of WT *C. reinhardtii* cells. (f) Optical image of a suspension of WT *C. reinhardtii* cells, with average density $\bar{\rho} = 0.49$ [scale bar, 50 microns]; pseudocolor plots of (g) the density and (h) the vorticity ω [colour-bar unit sec^{-1}] fields, for the image shown in (f). Panels (i), (j), and (k) are the *mbo2* *C. reinhardtii* counterparts of (f), (g), and (h), respectively. For the spatiotemporal evolution of (f)-(k) see the videos V1-V5 in the Supplementary Information.

slowing down as $\bar{\rho}$ increases, but they do not display all the characteristic properties of an active glass.

II. STATISTICAL CHARACTERISATION OF DENSE ALGAL SUSPENSIONS

In Fig. 1 we illustrate the two algal systems we consider. Wild type (WT) *C. reinhardtii* is a *contractile*

swimmer, on beat-averaged time scales and in the far-field limit [Figs. 1(a) and (c)]: it pulls the fluid from its front and back and pushes the fluid out from its sides. The two flagella of WT *C. reinhardtii* beat in a breast-stroke fashion as they propel the swimmer forward [Fig. 1(a)]. We compare and contrast the active turbulence of WT cells with that of the mutant *mbo2* *C. reinhardtii*, whose cells swim at a significantly lower speed ($v_m \simeq 50 \mu\text{m/s}$) than those of WT *C. reinhardtii*,

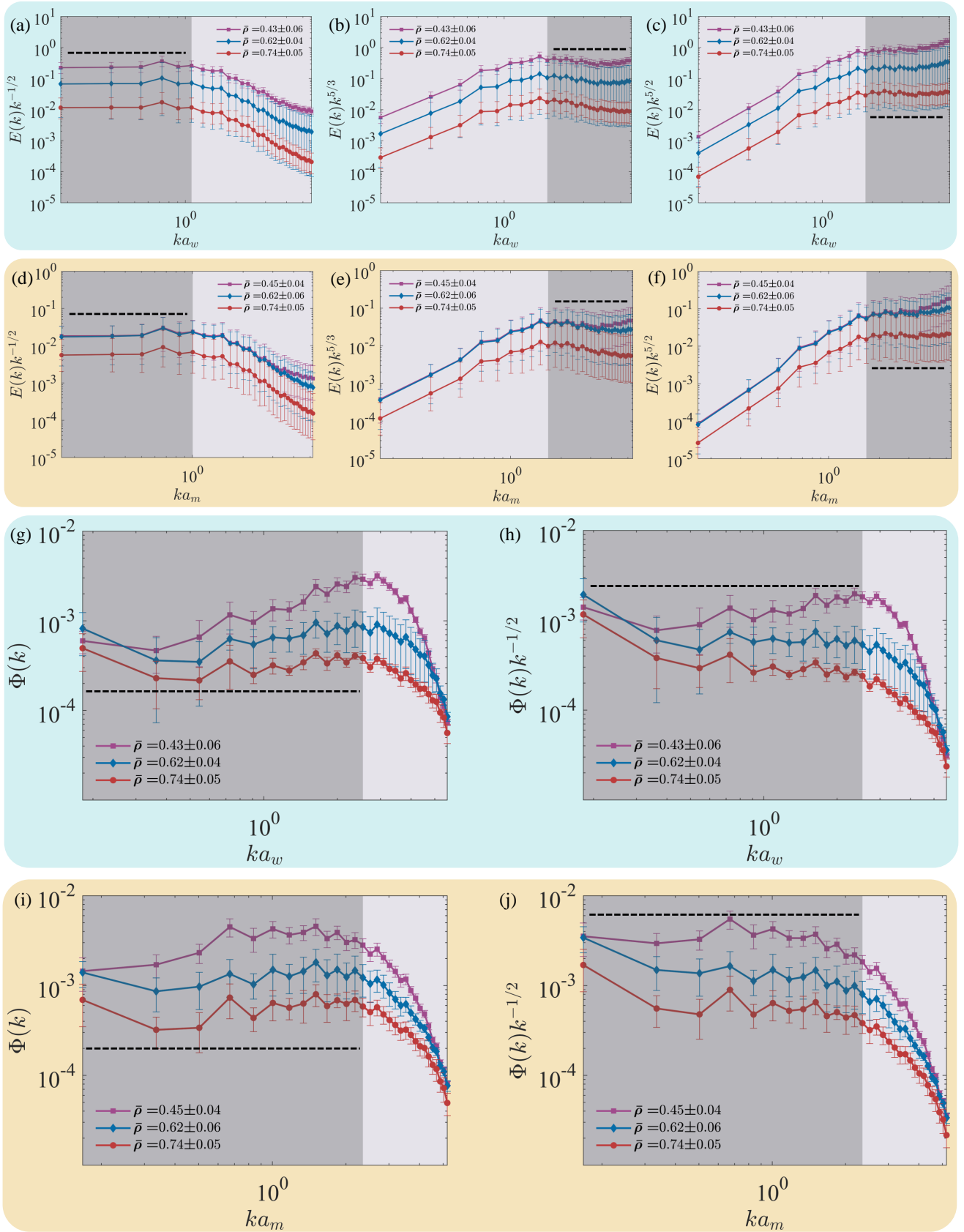


FIG. 2. Log-log plots of the energy spectra $E(k)$, compensated by different powers of k and plotted versus: (a)-(c) ka_w for WT cells with $\bar{\rho} = 0.43, 0.62, 0.74$; and (d)-(f) ka_m for mbo2 cells with $\bar{\rho} = 0.45, 0.62, 0.74$. Similar plots of concentration spectra $\Phi(k)$, compensated by different powers of k , are given in (g)-(h) for WT cells and (i)-(j) for mbo2 cells. These plots are consistent with $E(k) \sim k^{\alpha_1}$, for $ka_w \lesssim 1$, $0.4 \lesssim \bar{\rho} \lesssim 0.8$ and $\alpha_1 \simeq \frac{1}{2}$; $E(k) \sim k^{\alpha_2}$, for $2 \lesssim ka_w$, $0.7 \lesssim \bar{\rho} \lesssim 0.8$ and $\alpha_2 \simeq \frac{-5}{2}$; $E(k) \sim k^{\alpha_3}$, for $2 \lesssim ka_w$, $0.4 \lesssim \bar{\rho} \lesssim 0.5$ and $\alpha_3 \simeq \frac{-5}{3}$. $\Phi(k) \sim k^{\alpha_4}$, for $ka_w, ka_m \lesssim 2$, $\bar{\rho} \gtrsim 0.5$ and $\alpha_4 \simeq 0$; $\Phi(k) \sim k^{\alpha_5}$, for $ka_w, ka_m \gtrsim 2$, $\bar{\rho} \lesssim 0.5$ and $\alpha_5 \simeq \frac{1}{2}$. Dark-gray shading indicates scaling regions. Our data are averaged over different samples with similar values of $\bar{\rho}$ (within $\simeq 10\%$ of the mean); the error bars in $E(k)$ denote the maximal and the minimal values (at any given value of k); the error-bars in $\Phi(k)$ denote one-standard-deviation (ς), i.e., $\pm\varsigma(\Phi(k))$ and $\pm\varsigma(\Phi(k)k^{\frac{-1}{2}})$.

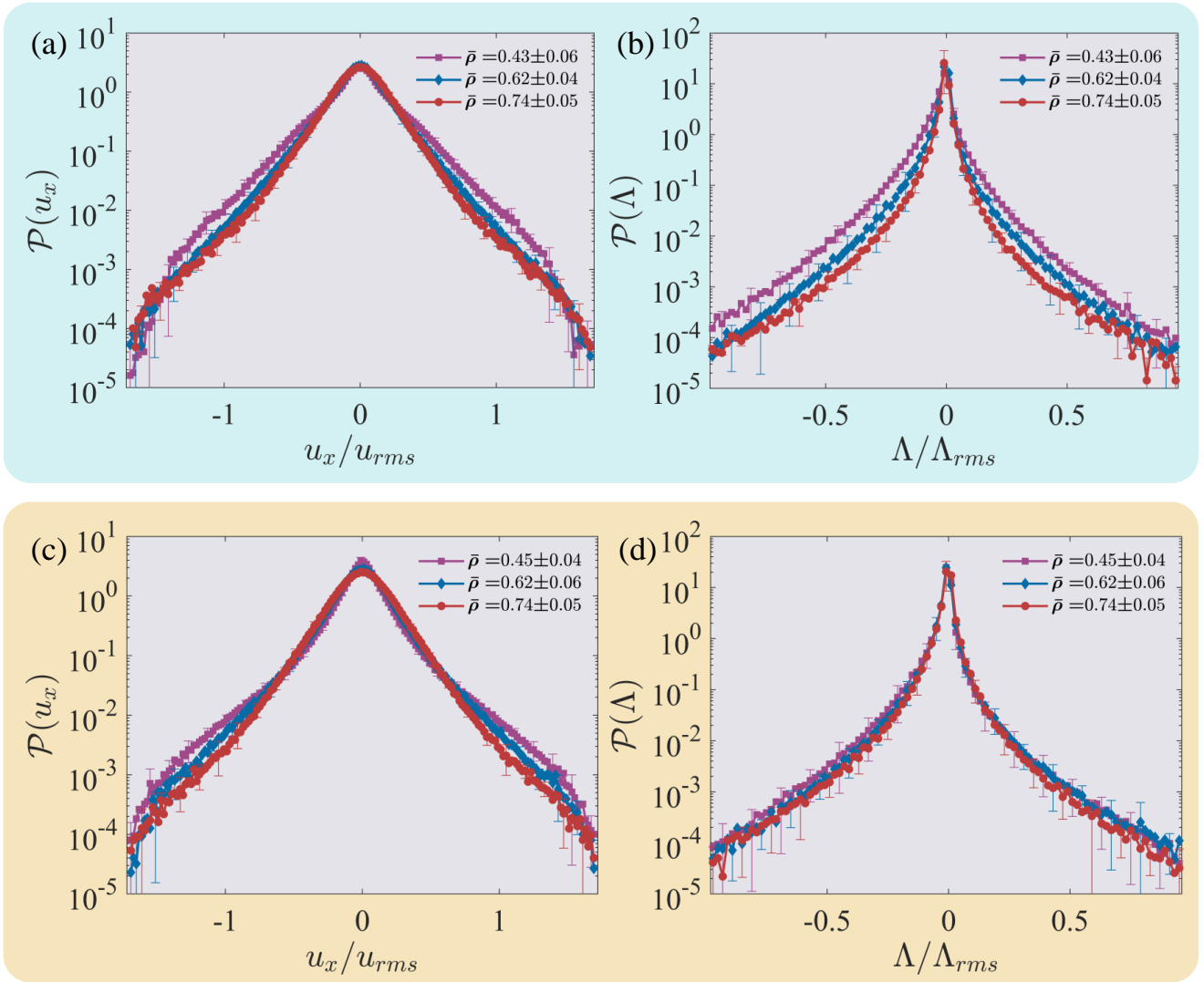


FIG. 3. Semilog plots of different probability distribution functions (PDFs): PDFs of (a) the x -component of the velocity field \mathbf{u} and (b) the Okubo-Weiss parameter Λ [see Eq. (10)] for WT *C. reinhardtii* cells and different mean densities $\bar{\rho}$. Panels (c) and (d) are the mbo2 *C. reinhardtii* counterparts of (a) and (b), respectively. Our data are averaged over different samples with similar values of $\bar{\rho}$ (within $\simeq 10\%$ of the mean); the error bars denote $\pm_{\zeta}(\mathcal{P}(u_x))$ and $\pm_{\zeta}(\mathcal{P}(\Lambda))$.

($v_w \simeq 100 \mu\text{m/s}$) and are effectively rear propelled by the flagella. The beat-averaged flow field of mbo2 cells resembles that of an *extensile* swimmer in the far-field limit [Figs. 1(b), (d)]. We focus on collections of such swimmers, confined to a quasi-two-dimensional (2D) domain, wherein the cells swim in a wide chamber with a depth that is comparable to, but slightly larger than, the cell diameter [Materials and Methods]. This allows us to visualize the spatiotemporal evolution of a monolayer of freely swimming *C. reinhardtii* cells. The swimmers collectively churn the fluid, which leads to an emergent chaotic flow, with more complex vortical fields than those generated by individual swimmers. We characterise this complexity systematically using statistical measures that

are employed to analyse statistically homogeneous and isotropic turbulence in fluids (see below). Figure 1(e) shows an optical image of the swimmers, at a representative time, overlaid with velocity vectors of the flow field obtained using PIV, whose magnitude is given by the colour that goes from blue (low speed) to red (high speed). We monitor the distributions of cells in dense suspensions of *C. reinhardtii*, and show these in Fig. 1 for WT cells (here and henceforth in a blue panel) and the mbo2 mutant (here and henceforth in a beige panel). Figure 1(f) shows a microscopic snapshot of a WT suspension with an average density $\bar{\rho} = 0.49$, at a representative time. At the same instant, we show a pseudocolor plot of the density field ρ , which lies between 0 (no cell

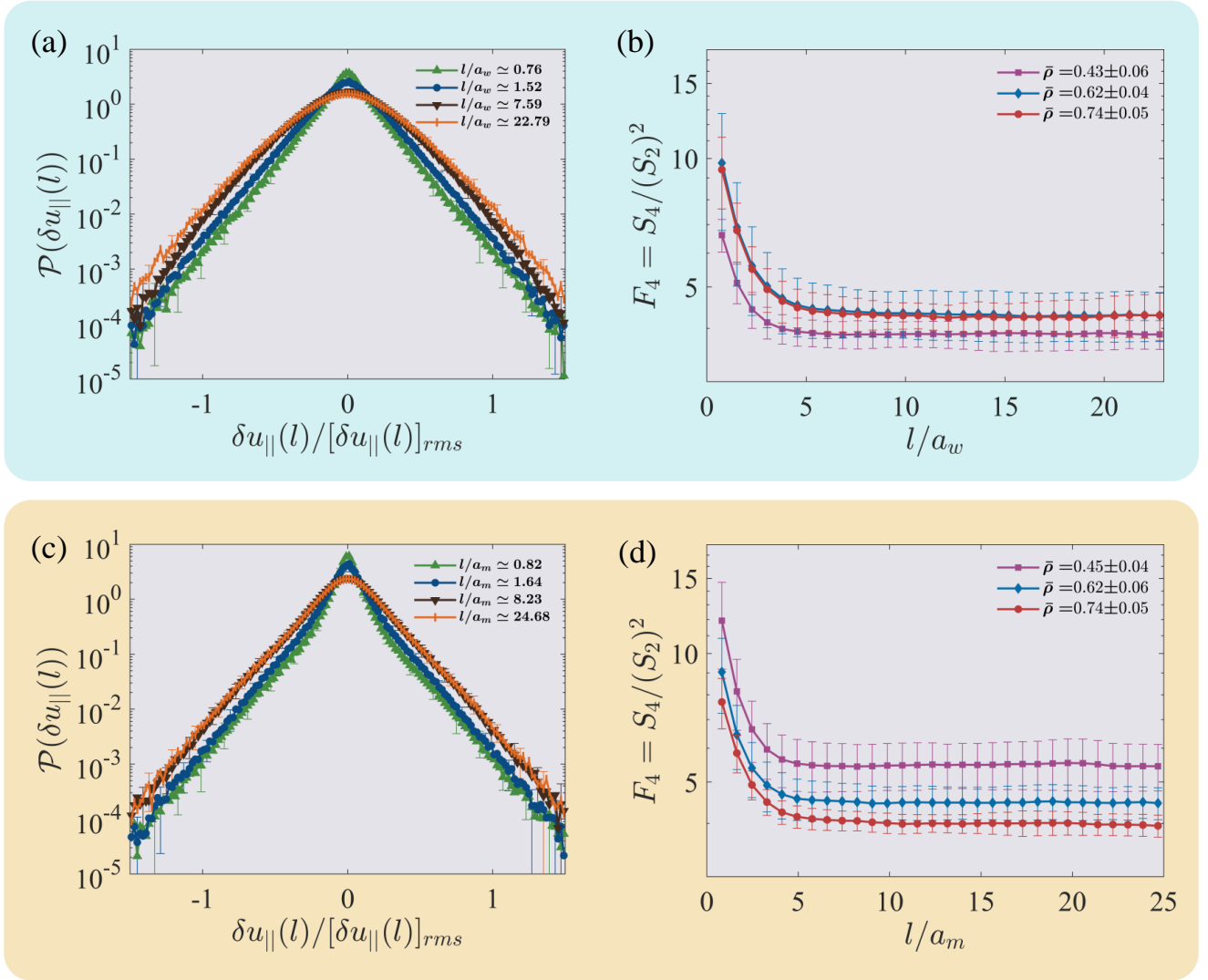


FIG. 4. Semilog plots, for WT *C. reinhardtii* cells, of (a) the PDFs of longitudinal-velocity increment of the velocity field \mathbf{u} , for different values of the separation l and the mean density $\bar{\rho} = 0.43 \pm 0.06$, and (b) the flatness F_4 [see Eq. (11)] versus l/a_w for different values $\bar{\rho}$. The plots in (c) and (d) are the mbo2-mutant counterparts of those in (a) and (b), respectively. Our data are averaged over different samples with similar values of $\bar{\rho}$ (within $\approx 10\%$ of the mean); the error bars denote $\pm\varsigma(\mathcal{P}(\delta\mathbf{u}_{||}(l)))$ and $\pm\varsigma(F_4)$.

present) and 1 (complete coverage with the cell bodies [Fig. 1(g)] and the vorticity-field ω computed from the velocity field \mathbf{u} [Fig. 1(h)]. The vorticity plots reveal higher magnitudes of the vorticity for the WT cells in comparison to their mbo2 variants; this arises principally from the differences in their swimming speeds. Figures 1 (i), (j), and (k) are, respectively, the counterparts of Figs. 1 (f), (g), and (h) for the mbo2 mutant. These plots and the videos V1-V5 show that dense suspensions of both WT and mbo2 *C. reinhardtii* cells show *emergent nonequilibrium states* that appear to display *spatiotemporal chaos* and a type of *turbulence*. We quantify the statistical properties of these states below.

In Fig. 2 we present log-log plots versus the wavenum-

ber k of the energy and concentration spectra, $E(k)$ and $\Phi(k)$, respectively [Eqs. (6)-(8) in Subsection IV E], for the wild-type (blue panels) and mbo2 mutant (beige panels). We compensate these spectra with different powers of k to uncover different power-law regimes; and we use a_w (a_m), the mean wild-type (mbo2-mutant) cell size (see Fig. 1 in the Supplementary Information) to non-dimensionalise k . The energy spectra scale as $E(k) \sim k^{1/2}$ in the $k \rightarrow 0$ limit for all $\bar{\rho}$ and for both types of swimmers. In the high-wavenumber limit, we observe an interesting transition in $E(k)$ as we vary $\bar{\rho}$. For $\bar{\rho} \approx 0.4$, the spectrum follows $E(k) \sim k^{-5/3}$, which steepens to $E(k) \sim k^{-5/2}$ as the density increases. This transition is observed for both types of swimmers.

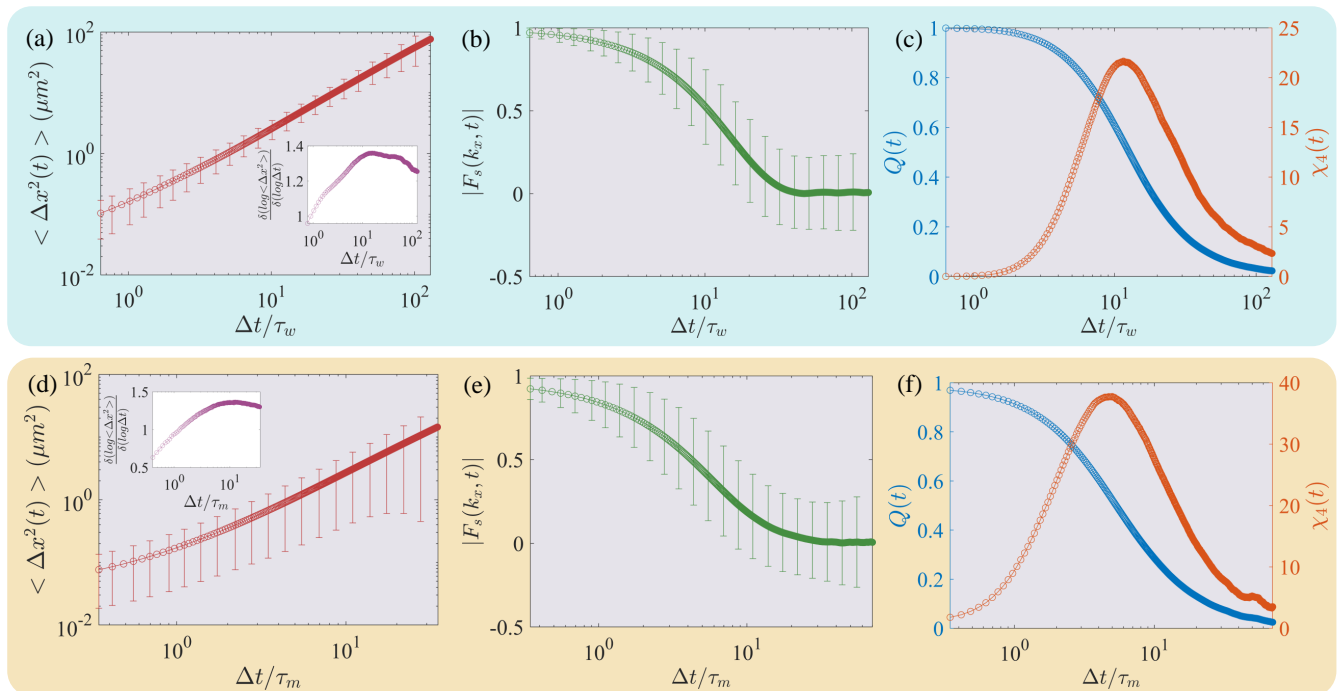


FIG. 5. Plots versus the scaled time $\Delta t/\tau_w$ of (a) the mean-square displacement (MSD) [the local slope $\frac{\delta(\log \langle \Delta x^2 \rangle)}{\delta(\log \Delta t)}$ is shown in the inset], (b) the modulus $|F_s(k_x, t)|$ of the self-intermediate-scattering function (for $k_x a_w = 8.35$), and (c) the self-overlap function $Q(t)$ and the four-point correlation function $\chi_4(t)$ [see Eqs.(12), (13), (14), (15)] for WT *C. reinhardtii* cells with $\bar{\rho} = 0.74 \pm 0.05$; the reference time scale τ_w is defined in the text; (d), (e) and (f) are the mbo2-mutant counterparts of those in (a), (b) and (c), respectively. Our data are averaged over cell-trajectories of samples with similar values of $\bar{\rho}$ (within $\simeq 10\%$ of the mean); the error bars denote $\pm \zeta(\Delta x^2(t))$ and $\pm |\zeta(F_s(k_x, t))|$.

Although the exponent $-5/3$ is reminiscent of the exponent for the inverse-cascade scaling regime in high-Reynolds-number 2D fluid turbulence [4, 5] and in low-Reynolds-number active-scalar turbulence [26], there are significant differences between our spectra and their 2D-fluid-turbulence counterparts [see, e.g., Ref. [4, 5]]. In brief, a conventional 2D fluid yields statistically homogeneous and isotropic turbulence, if it is forced sufficiently strongly at a length scale l_f ; the resulting energy spectrum displays two spectral regimes – the first with an *inverse cascade* of energy and the second with a *forward cascade* of enstrophy (i.e., the mean-square vorticity); in the inverse-cascade regime $E(k) \sim k^{-5/3}$, whereas, in the forward-cascade regime, $E(k) \sim k^{-\varpi}$, with $\varpi = 3$ in the absence of friction [3, 4]; the crossover between these two regimes occurs at a wavenumber $k_f \simeq 2\pi/l_f$. Energy spectra for bacterial turbulence are also markedly different from those that we find for algal turbulence; e.g., the simple Toner-Tu-Swift-Hohenberg (TTSH) model, which has been used to model bacterial turbulence in *Bacillus subtilis* and *Escherichia coli*, yields a low- k power-law regime in $E(k)$, but with an activity-dependent spectral exponent [10] that saturates eventually to a value $\simeq -3/2$ at large activity [27].

The density spectrum $\Phi(k) \sim k^{1/2}$ at low wave numbers for low densities; and it approaches a constant for

large densities, as shown in Fig. 2.

Figures 3(a) and (b) [blue panel] present PDFs (denoted generically by \mathcal{P}) of (a) \mathbf{u}_x and (b) the Okubo-Weiss parameter [5, 28, 29] Λ [see Materials and Methods, Eq. (10)] of WT cell suspensions. Their counterparts for the mbo2 mutant are given, respectively, in Figs. 3(c) and (d) [beige panel]. The PDFs for the wild-type system are qualitatively similar to their counterparts in the mbo2-mutant systems; however, quantitative differences do appear, especially in the PDFs for Λ . Moreover, $\mathcal{P}(\Lambda)$ shows more dependence on $\bar{\rho}$ for the WT cells than it does for the mbo2 variant.

Note that the PDFs of \mathbf{u}_x are *markedly different* from those that are obtained for conventional fluid turbulence [see, e.g., Ref. [5]] and bacterial turbulence in dense suspensions of *Bacillus subtilis* [see, e.g., Ref. [9]], both of which are Gaussian. By contrast, the PDFs of \mathbf{u}_x , in Figs. 3(a) and (c), are distinctly non-Gaussian (we give fits to sums of exponentials and compressed exponentials in the Supplementary Information in Fig. 2). Furthermore, $\mathcal{P}(\Lambda)$ in the algal-turbulence state of our dense suspensions of *C. reinhardtii* cells is significantly different from its counterparts in 2D fluid turbulence [30] and bacterial turbulence [13].

Figure 4(a) [blue panel] displays PDFs (\mathcal{P}) of the longitudinal velocity increments $\delta \mathbf{u}_{\parallel}(l)$ of WT cell suspen-

sions [5] [see Materials and Methods, Eq. (9)] for different values of l ; Fig. 4(c) [beige panel] gives these PDFs for the mbo2 mutant. The l -dependence of these velocity-increment PDFs is a fingerprint of intermittency, which we quantify by the flatness F_4 that is related to the fourth- and second-order velocity structure functions [see Materials and Methods, Eq. (11)]. We plot the flatness, F_4 for both WT (versus l/a_w) and mbo2 (versus l/a_m) variants, in Figs. 4 (b) and 4 (d), respectively. Both these plots show distinct deviations from the Gaussian value $F_4^G = 3$; this deviation increases as l/a_w (or l/a_m) decreases, a clear manifestation of small-scale intermittency in the algal turbulence we consider [31]. Furthermore, F_4 shows more dependence on $\bar{\rho}$ for the mbo2 mutant than it does for the WT variant, even though the error bars are large.

We turn now to an investigation of possible signatures of an active glass in our WT and mbo2 systems at large values of $\bar{\rho}$. Figures 5 (a), (b), and (c) show, respectively, plots of the mean-square displacement (MSD), the modulus $|F_s(k_x, t)|$ of the self-intermediate-scattering function (for $k_x a_w = 8.35$), the self-overlap function $Q(t)$, and the four-point correlation function $\chi_4(t)$ versus the scaled time $\Delta t/\tau_w$ [see Eqs.(12), (13), (14), (15)] for WT *C. reinhardtii* cells with $\bar{\rho} = 0.74$; the reference time scale $\tau_w \equiv a_w/v_w$, where $v_w \simeq 100 \mu\text{m/s}$ is the mean swimming speed of isolated WT cells; the local slope $\frac{\delta(\log\langle\Delta x^2\rangle)}{\delta(\log\Delta t)}$ is shown in the inset of Fig. 5 (a). Figures 5 (d), (e), and (f) are the mbo2 counterparts of Figs. 5 (a), (b), and (c); for mbo2, $k_x a_m = 15.41$ and the reference time scale $\tau_m \equiv a_m/v_m$, where $v_m \simeq 50 \mu\text{m/s}$ is the mean swimming speed of isolated mbo2 cells. We observe that there are no well-developed plateaux in the plots of the MSD, $F_s(k, t)$, and $Q(t)$; such plateaux are desiderata for an active glass [23]. However, the presence of a peak in the four-point correlation function $\chi_4(t)$ suggests dynamic heterogeneity in our algal systems.

III. ALGAL TURBULENCE VERSUS AN ACTIVE ALGAL GLASS

We have uncovered a new type of emergent active turbulence in dense algal systems of two types of *C. reinhardtii* cells. This algal turbulence displays power-law energy spectra and signatures of small-scale intermittency that are qualitatively similar to their counterparts in conventional fluid turbulence [see, e.g., Refs. [4, 5]] and in bacterial turbulence, which has garnered considerable attention over the past decade [see, e.g., Refs. [7, 9, 13, 27]]. However, there are important quantitative differences between the algal turbulence, which we investigate, and fluid and bacterial turbulence. We have characterised these differences by computing various statistical properties of algal turbulence.

Microswimmer turbulence is often associated with the presence of topological defects and orientational instabilities and, therefore, is limited to rod-shaped bacteria.

Our study shows that turbulence can also arise in the absence of orientational instabilities and hence is a universal feature of free-swimming micro-organisms, regardless of their shape.

Reference [26], which has carried out a theoretical and numerical study of the active Cahn Hilliard Navier Stokes (CHNS) equations, suggests that active-scalar turbulence in this system might be realised in dense suspensions of *C. reinhardtii*. The two-dimensional (2D) active CHNS model they consider for a dense suspension of contractile swimmers [15, 32] is:

$$\partial_t \phi + (\mathbf{u} \cdot \nabla) \phi = M \nabla^2 \left(\frac{\delta \mathcal{F}}{\delta \phi} \right); \quad (1)$$

$$\partial_t \omega + (\mathbf{u} \cdot \nabla) \omega = \nu \nabla^2 \omega + \frac{3}{2} \epsilon \nabla \times (\nabla \cdot \Sigma^A) - \alpha \omega; \quad (2)$$

$$\nabla \cdot \mathbf{u} = 0; \quad (3)$$

the vorticity $\omega = \nabla \times \mathbf{u}$ and M , ν , and α are, respectively, the mobility, kinematic viscosity, and bottom friction, and the Landau-Ginzburg variational free-energy functional is

$$\mathcal{F}[\phi, \nabla \phi] = \int_{\Omega} \left[\frac{3}{16} \frac{\sigma}{\epsilon} (\phi^2 - 1)^2 + \frac{3}{4} \sigma \epsilon |\nabla \phi|^2 \right]; \quad (4)$$

the first term in the integrand has minima at $\phi = \pm 1$; and the scalar ϕ is, respectively, positive where the microswimmer density is high and negative where this density is low; ϕ varies smoothly across interfaces between these regions. The bare surface tension σ measures the free-energy cost for an interface, whose width $\sim \epsilon$. In this active model, all terms in the stress tensor cannot be derived from \mathcal{F} ; the stress tensor Σ^A has the components [15, 32–34]

$$\Sigma_{ij}^A = -\zeta \left[\partial_i \phi \partial_j \phi - \frac{\delta_{ij}}{2} |\nabla \phi|^2 \right]; \quad (5)$$

ζ , the activity coefficient, is negative for contractile swimmers [32] but positive for their extensile counterparts. The density in the algal suspension depends on ϕ ; in particular, $\rho(\phi) \equiv \rho_1(1 + \phi)/2 + \rho_2(1 - \phi)/2$, where ρ_1 and ρ_2 are the densities of the algal-rich and algal-poor regions.

A comparison of our results for $E(k)$ and $\Phi(k)$ with those of Ref. [26] [see Figs. 3(a) and (b) there] shows a qualitative similarity between these spectra, but the exponents, which characterise the power-law spectral regimes, are not the same. Furthermore, the active-CHNS system yields a turbulent state only for contractile swimmers; here, we find turbulence for both the WT and mbo2 cells; this discrepancy might arise because WT and mbo2 cells are contractile or extensile only on average, as the flagellar stroke during a beat cycle varies [35]. Therefore, the theoretical modelling of algal turbulence in dense suspensions of *C. reinhardtii* cells is still a challenging, open problem; to the extent that our results for WT and mbo2 variants are qualitatively similar, we

might well have to go beyond models, like the one proposed in Ref. [26], that yield qualitatively different results for contractile and extensile microswimmers.

In summary, we have demonstrated that, at low values of $\bar{\rho}$, our algal systems display an emergent nonequilibrium state with statistically steady algal turbulence. Although this algal turbulence decreases, with increasing $\bar{\rho}$, it does not cross over completely to a state that can be identified as a *bona fide* active algal glass. It might well turn out that our dense suspensions of *C. reinhardtii* cross over to an active algal glass at values of $\bar{\rho}$ that are larger than those we have considered here; however, such high densities are hard to achieve in experiments, so the explorations of active glassy dynamics in very dense suspensions of *C. reinhardtii* remains a challenge for future studies. Furthermore, algal turbulence has obvious biological implications; such turbulence enhances mixing and transport, so we conjecture that it aids *C. reinhardtii* in foraging for and outrunning diffusing nutrient molecules.

IV. MATERIALS AND METHODS

A. Cell culture

Chlamydomonas reinhardtii cells of both the WT and mbo2 strains are inoculated from agar plates into TAP+P media and grown at 25° Celsius in 12:12 hour day-night cycles inside an orbital shaker at 137rpm [36]. When the cells are in the logarithmic phase of their growth cycle, the culture is collected in Eppendorf tubes and then centrifuged multiple times (at 0.3rcf for 4 minutes) to obtain samples with different cell concentrations.

C. reinhardtii is a photosynthetic alga that feeds on dissolved inorganic ions or molecules that are in the TAP+P media; these include phosphate and ammonium ions and carbon dioxide from the surrounding fluid; light is the main source of energy [see, e.g., Refs. [37, 38]]. The macronutrients that limit algal metabolism and growth are nitrogen and carbon [see, e.g., Refs. [38–40]]. Flow fields that are flagella-driven help to distribute these dissolved solute molecules uniformly through fluid mixing and transport [see, e.g., Refs. [17, 19, 37, 38, 40, 41]].

B. Surface modification of glass slides, cover slips and beads

A polyacrylamide brush is coated on the glass slides and cover slips to avoid non-specific adhesion of cells and beads on the glass surfaces [42]. Also, the microspheres (Sulphate latex 200nm beads, Thermofisher) are coated with PLL-PEG to impart steric stabilization, thereby reducing inter-particle aggregation and obtaining mono-dispersed microspheres in the media [42].

C. Microscopic imaging

Double-sided tape of height 10 micron (Nitto Denko Corporation) is used as a spacer between the coverslip and the glass slide to obtain the chambers in which the cell-culture is placed (Supplementary Information Section 2). The sample is kept under an inverted microscope (Olympus IX83) coupled with a CMOS high-speed camera (Phantom Miro C110, Vision Research, Pixel size = 5.6 micron). Different concentrations of both the WT and mbo2 mutant cells are imaged under red-light (> 610nm) using a 20x objective in bright field at 100 fps. Dilute cultures are mixed with 200nm microspheres and then imaged using a 60x phase objective at 500 fps to obtain flow fields of isolated cells [43].

D. Obtaining PIV, Cell Density, and Flow-fields from the images

The velocity vectors are obtained using the Matlab tool PIVlab [44] with a time interval of 50ms between successive frames. We use the FFT window deformation algorithm and two passes to analyze the images. For the first pass, we use an interrogation window of size $16.8\mu m$, and the second pass has a size of $8.4\mu m$. We follow the bacterial-suspension studies of Refs. [9, 45], in which bacteria are used as tracers; here, PIV tracks bacterial flow, instead of the fluid flow; nevertheless, the fluid and bacterial flows have been found to share quantitatively similar statistical structures [9, 45]. We use PIV to track algal flows and assume, as in Refs. [9, 45], that the algal and fluid flows are statistically similar. The spatial cell density is determined by calculating the area fraction covered by the cells at a particular location for each frame (Fig.3, Supplementary Information). Particle tracking velocimetry (PTV), wherein individual microspheres are tracked to calculate their velocity vectors, was used to compute the beat averaged flow fields of isolated WT and mbo2 cells [43].

E. Statistical measures for algal turbulence

The statistical properties that we use to explore active turbulence in our system are given below:

- The instantaneous concentration and energy spectra are, respectively:

$$\Phi(k, t) = \frac{1}{2} \sum_{k-\frac{1}{2} \leq k' \leq k+\frac{1}{2}} [\hat{\rho}(\mathbf{k}', t) \hat{\rho}(-\mathbf{k}', t)]; \quad (6)$$

$$E(k, t) = \frac{1}{2} \sum_{k-\frac{1}{2} \leq k' \leq k+\frac{1}{2}} [\hat{\mathbf{u}}(\mathbf{k}', t)] \cdot [\hat{\mathbf{u}}(-\mathbf{k}', t)]; \quad (7)$$

here, carets denote spatial Fourier transforms, and k and k' are the moduli of the wave vectors \mathbf{k} and \mathbf{k}' .

- In the statistically steady state, we obtain the averaged spectra

$$\Phi(k) = \langle \Phi(k, t) \rangle_t; \quad E(k) = \langle E(k, t) \rangle_t; \quad (8)$$

here, $\langle \cdot \rangle_t$ is the time average; typically we take the mean over $\simeq 800$ spectra, obtained from configurations of the density and velocity fields, at well-separated times in the nonequilibrium statistically steady state. We also average over different samples with similar densities [see Fig. 2].

- For various PDFs, we also compute the x -component of the velocity field \mathbf{u} and the longitudinal velocity increments

$$\delta \mathbf{u}_{\parallel}(\mathbf{x}, l, t) \equiv [\mathbf{u}(\mathbf{x} + \mathbf{l}, t) - \mathbf{u}(\mathbf{x}, t)] \cdot \frac{\mathbf{l}}{l}, \quad (9)$$

for different length scales l .

- Furthermore, we compute the Okubo-Weiss parameter [5, 28, 29]

$$\begin{aligned} \Lambda &= \Omega^2 - D^2; \quad D = \frac{\nabla \mathbf{u} + \nabla \mathbf{u}^T}{2}; \\ \Omega &= \frac{\nabla \mathbf{u} - \nabla \mathbf{u}^T}{2}; \end{aligned} \quad (10)$$

D and Ω are the rate-of-deformation and rate-of-rotation tensors, respectively; $\Lambda > 0$ in strain-dominated regions of the flow and $\Lambda < 0$ in vortical regions.

- We compute the flatness $F_4(l)$ to check for intermittency in our system [1, 5, 46, 47]:

$$\begin{aligned} F_4(l) &= \frac{S_4(l)}{(S_2(l))^2}; \\ S_p(l) &= \langle [\delta \mathbf{u}_{\parallel}(\mathbf{x}, l, t)]^p \rangle_{\mathbf{x}, t}; \end{aligned} \quad (11)$$

here, $S_p(l)$ is the longitudinal-velocity structure function and $\langle \cdot \rangle_{\mathbf{x}, t}$ denotes the average over the spatial origin \mathbf{x} and the time t .

F. Statistical measures for active glasses

In the active-glass literature [see, e.g., Ref. [23]] various statistical properties are used to characterise a glass. The analysis that we present here is based on the particles (here, *C. reinhardtii* cells) that comprise the glass;

by contrast, our analysis of turbulence in the previous Section is based on density and velocity fields of the type that are used in hydrodynamical models of active-scalar turbulence [26]. The statistical properties that we use to explore the formation of an active glass in our system are given below:

- The mean-square displacement (MSD)

$$\langle \Delta x^2(t) \rangle = \left\langle \frac{1}{N} \sum_{i=1}^N [\mathbf{x}_i(t+t_0) - \mathbf{x}_i(t_0)]^2 \right\rangle_{t_0}; \quad (12)$$

here, $\mathbf{x}_i(t)$ is the position of the i^{th} cell at time t and N is the total number of cells. We use $N \simeq 1000 - 1500$.

- The self intermediate scattering function $F_s(\mathbf{k}, t)$, at wave vector \mathbf{k} and time t ,

$$F_s(\mathbf{k}, t) = \left\langle \frac{1}{N} \sum_{i=1}^N e^{i\mathbf{k} \cdot (\mathbf{x}_i(t+t_0) - \mathbf{x}_i(t_0))} \right\rangle_{t_0}; \quad (13)$$

in our calculations we use $\mathbf{k} = k_x \hat{\mathbf{x}}$.

- The overlap function

$$\begin{aligned} \tilde{Q}_i &= \langle W(a - |\mathbf{x}_i(t+t_0) - \mathbf{x}_i(t_0)|) \rangle_{t_0}; \\ Q(t) &= \frac{1}{N} \sum_{i=1}^N \tilde{Q}_i \equiv \langle \tilde{Q}_i \rangle_i; \end{aligned} \quad (14)$$

where W is the Heaviside step function and the length scale a is taken as the typical vibrational amplitude of the glass particles; in our systems, we chose a such that $a/a_w = 0.18$ for the WT cells and $a/a_m = 0.097$ for the mbo2 mutant.

- The four-point correlation function

$$\chi_4(t) = N[\langle \tilde{Q}_i^2 \rangle_i - \langle \tilde{Q}_i \rangle_i^2]; \quad (15)$$

V. ACKNOWLEDGMENTS

P.V.B and P.S thank the ANRF grant CRG/2022/000724 and the CSIR grant 03WS(008)/2023-24/EMR-II/ASPIRE for providing the support to carry out the experiments. N.B.P., B.M., and R.P thank K.V. Kiran for discussions, the Anusandhan National Research Foundation (ANRF), the Science and Engineering Research Board (SERB), and the National Supercomputing Mission (NSM), India, for support, and the Supercomputer Education and Research Centre (IISc), for computational resources.

[1] U. Frisch, *Turbulence: The Legacy of A. N. Kolmogorov* (Cambridge University Press, 1996).

[2] D. Biskamp, *Magnetohydrodynamic turbulence* (Cambridge University Press, 2003).

- [3] R. Pandit, P. Perlekar, and S. S. Ray, *Pramana* **73**, 157 (2009).
- [4] G. Boffetta and R. E. Ecke, *Annual review of fluid mechanics* **44**, 427 (2012).
- [5] R. Pandit, D. Banerjee, A. Bhatnagar, M. Brachet, A. Gupta, D. Mitra, N. Pal, P. Perlekar, S. S. Ray, V. Shukla, *et al.*, *Physics of fluids* **29**, 111112 (2017).
- [6] R. Benzi and F. Toschi, *Physics Reports* **1021**, 1 (2023).
- [7] R. Alert, J.-F. Joanny, and J. Casademunt, *Nature Physics* **16**, 682 (2020).
- [8] H. H. Wensink, J. Dunkel, S. Heidenreich, K. Drescher, R. E. Goldstein, H. Löwen, and J. M. Yeomans, *Proceedings of the National Academy of Sciences* **109**, 14308 (2012).
- [9] J. Dunkel, S. Heidenreich, K. Drescher, H. H. Wensink, M. Bär, and R. E. Goldstein, *Phys. Rev. Lett.* **110**, 228102 (2013).
- [10] V. Bratanov, F. Jenko, and E. Frey, *Proceedings of the National Academy of Sciences* **112**, 15048 (2015).
- [11] L. Wang and Y. Huang, *Phys. Rev. E* **95**, 052215 (2017).
- [12] R. Alert, J. Casademunt, and J.-F. Joanny, *Annual Review of Condensed Matter Physics* **13**, 143 (2022).
- [13] K. V. Kiran, A. Gupta, A. K. Verma, and R. Pandit, *Phys. Rev. Fluids* **8**, 023102 (2023).
- [14] N. B. Padhan and A. Voigt, *Journal of Physics: Condensed Matter* **37**, 105101 (2025).
- [15] N. B. Padhan and R. Pandit, *Physical Review Research* **5**, L032013 (2023).
- [16] D. Buaria and K. R. Sreenivasan, *Phys. Rev. Lett.* **131**, 204001 (2023).
- [17] K. C. Leptos, J. S. Guasto, J. P. Gollub, A. I. Pesci, and R. E. Goldstein, *Physical Review Letters* **103**, 198103 (2009).
- [18] J.-L. Thiffeault, *Physical Review E* **92**, 023023 (2015).
- [19] H. Kurtuldu, J. S. Guasto, K. A. Johnson, and J. P. Gollub, *Proceedings of the National Academy of Sciences* **108**, 10391 (2011), <https://www.pnas.org/doi/pdf/10.1073/pnas.1107046108>.
- [20] T. Dombre, U. Frisch, J. M. Greene, M. Hénon, A. Mehr, and A. M. Soward, *Journal of Fluid Mechanics* **167**, 353 (1986).
- [21] Z. Warhaft, *Annual Review of Fluid Mechanics* **32**, 203 (2000).
- [22] G. Falkovich, K. Gawedzki, and M. Vergassola, *Reviews of modern Physics* **73**, 913 (2001).
- [23] S. Sadhukhan, S. Dey, S. Karmakar, and S. K. Nandi, *The European Physical Journal Special Topics* , 1 (2024).
- [24] R. Mandal, P. J. Bhuyan, M. Rao, and C. Dasgupta, *Soft Matter* **12**, 6268 (2016).
- [25] S. Henkes, Y. Fily, and M. C. Marchetti, *Phys. Rev. E Stat. Nonlin. Soft Matter Phys.* **84**, 040301 (2011).
- [26] N. B. Padhan, K. V. Kiran, and R. Pandit, *Soft Matter* **20**, 3620 (2024).
- [27] S. Mukherjee, R. K. Singh, M. James, and S. S. Ray, *Nature Physics* , 1 (2023).
- [28] J. Weiss, *Physica D: Nonlinear Phenomena* **48**, 273 (1991).
- [29] A. Okubo, in *Deep sea research and oceanographic abstracts*, Vol. 17 (Elsevier, 1970) pp. 445–454.
- [30] P. Perlekar and R. Pandit, *New J. Phys.* **11**, 073003 (2009).
- [31] Signatures of small-scale intermittency are often uncovered by such plots of flatness or the hyperflatness $F_6 \equiv S_6/(S_2)^3$ in fluid and other forms of turbulence; see, e.g., Refs. [1, 5, 46, 47].
- [32] A. Tiribocchi, R. Wittkowski, D. Marenduzzo, and M. E. Cates, *Physical review letters* **115**, 188302 (2015).
- [33] J. K. Bhattacharjee and T. R. Kirkpatrick, *Phys. Rev. Fluids* **7**, 034602 (2022).
- [34] A. Das, J. K. Bhattacharjee, and T. R. Kirkpatrick, *Phys. Rev. E* **101**, 023103 (2020).
- [35] G. S. Klindt and B. M. Friedrich, *Phys. Rev. E* **92**, 063019 (2015).
- [36] S. K. Choudhary, A. Baskaran, and P. Sharma, *Biophys. J.* **117**, 1508 (2019).
- [37] D. Tam and A. E. Hosoi, *Proc. Natl. Acad. Sci. U. S. A.* **108**, 1001 (2011).
- [38] T. Kiørboe, *A Mechanistic Approach to Plankton Ecology* (Princeton University Press, 2008).
- [39] M. I. Khan, J. H. Shin, and J. D. Kim, *Microb. Cell Fact.* **17**, 36 (2018).
- [40] M. B. Short, C. A. Solari, S. Ganguly, T. R. Powers, J. O. Kessler, and R. E. Goldstein, *Proc. Natl. Acad. Sci. U. S. A.* **103**, 8315 (2006).
- [41] Y. Ding, J. C. Nawroth, M. J. McFall-Ngai, and E. Kanso, *J. Fluid Mech.* **743**, 124 (2014).
- [42] D. Mondal, R. Adhikari, and P. Sharma, *Science Advances* **6**, eabb0503 (2020), <https://www.science.org/doi/pdf/10.1126/sciadv.abb0503>.
- [43] D. Mondal, A. G. Prabhune, S. Ramaswamy, and P. Sharma, *eLife* **10**, e67663 (2021).
- [44] W. Thielicke and E. J. Stamhuis, *J. Open Res. Softw.* **2** (2014).
- [45] Z. Liu, W. Zeng, X. Ma, and X. Cheng, *Soft Matter* **17**, 10806 (2021).
- [46] P. Perlekar, D. Mitra, and R. Pandit, *Physical review letters* **97**, 264501 (2006).
- [47] G. Sahoo, P. Perlekar, and R. Pandit, *New Journal of Physics* **13**, 013036 (2011).

Supplementary Information

This Supplementary Information contains some details about the cells sizes of the two strains, height measurement of the sample chamber, fitted PDFs of the x component of the velocity and the longitudinal velocity increments, computations of the spatial density from the microscopic image, and a list of videos that show the spatiotemporal evolution of the CR cells and also of the pseudocolor plots in Figs. 1 (g), (h), (j), and (k) [in the main paper].

I. CELL SIZES OF DIFFERENT STRAINS

Figure 1 presents histograms of the mean diameters for both the Wild-type (WT) and the *mbo2* mutant *C. reinhardtii* cells. The average diameter of the WT cell is $a_w = 7.82 \pm 0.84 \mu\text{m}$ and for the *mbo2* cell $a_m = 7.22 \pm 0.85 \mu\text{m}$.

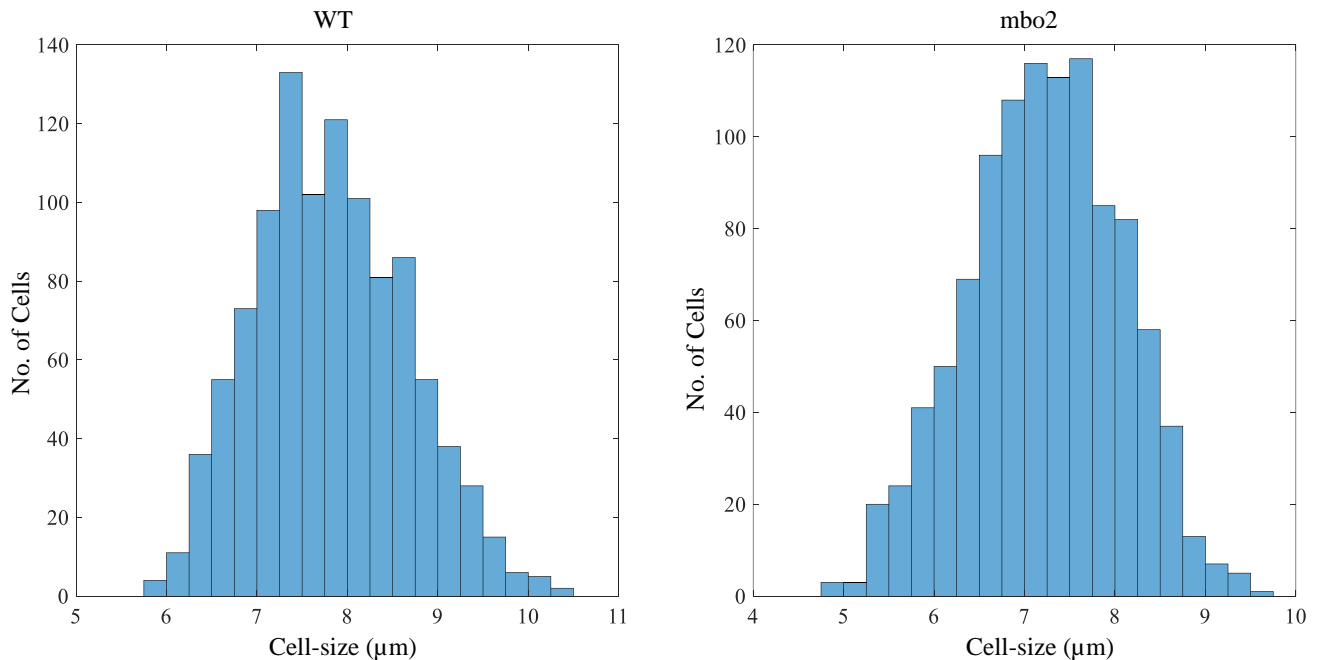


FIG. 1. Histogram plots of the cell-sizes for the wild-type cells (left) and the *mbo2* mutant(right)

II. HEIGHT MEASUREMENT OF THE CHAMBER

We take a dilute solution of microspheres (Sulphate latex 200nm beads, from Thermofisher) on the coverslip and the glass slide; we then heat the glass slide and the coverslip gently so that the beads get stuck on both the surfaces. After that, immersion oil is put into the sample chamber. We use a 60x oil-immersion phase objective to focus on the beads and determine the chamber height to be $10.27 \pm 0.61 \mu\text{m}$.

III. FITTED PDFS

We find that the PDFs [given in Figs. 3(a), 3(c), 4(a), and 4(c) in the main paper] can be fit to a form that is the sum of an exponential and a compressed exponential. Such fits are shown in Fig. 2. For example, for the WT cells, we obtain $\mathcal{P}(\mathbf{u}_x) = (1.01)e^{-22|\mathbf{u}_x|^{1.73}} + (2.09)e^{-6|\mathbf{u}_x|}$ for $\bar{\rho} = 0.62$.

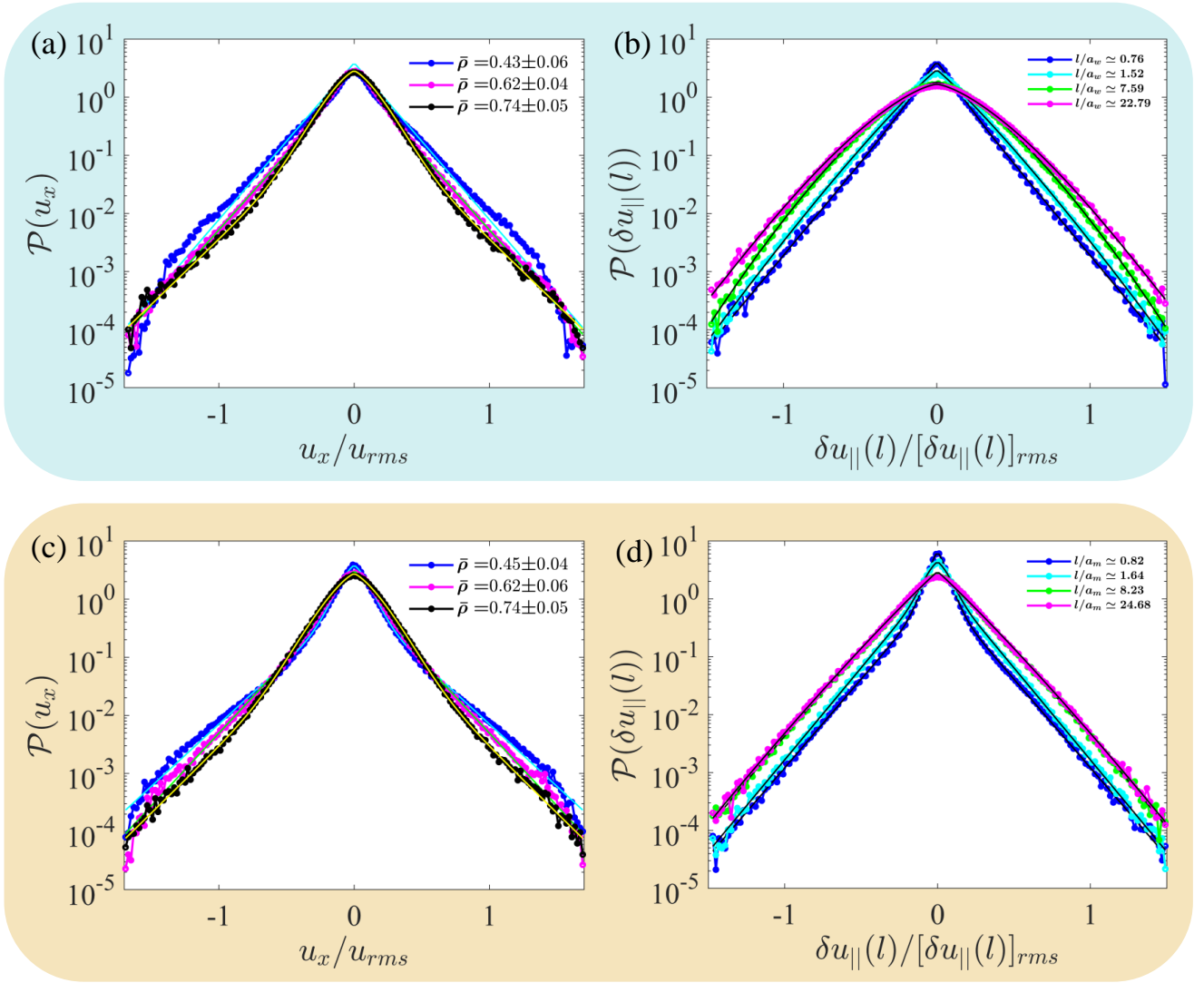


FIG. 2. Fitted PDFs of (a) the x -component of the velocity and (b) the longitudinal velocity increments for the WT cells. (c) and (d) are the mbo2 counterparts of (a) and (b).

IV. SPATIAL DENSITY FROM THE MICROSCOPIC IMAGE

We binarize the image in Fig. 3 such that the points, where the cells are present, are shown in white (pixel value = 1) and the background is black (pixel value = 0). To obtain the area fraction covered by the cells in a given region, we count the number of pixels occupied by the cells there and divide it by the total area of the region. This gives us the spatial cell-density of the suspension at a given instant of time.

V. VIDEOS

- V1: This experimental video shows the spatiotemporal evolution of WT cell suspensions with $\bar{\rho} = 0.49$. The video is captured with a Phantom Miro C110 Camera using a 20x bright field objective in an Olympus IX83 microscope.
- V2: This experimental video shows the spatiotemporal evolution of WT cell suspensions with $\bar{\rho} = 0.72$. The

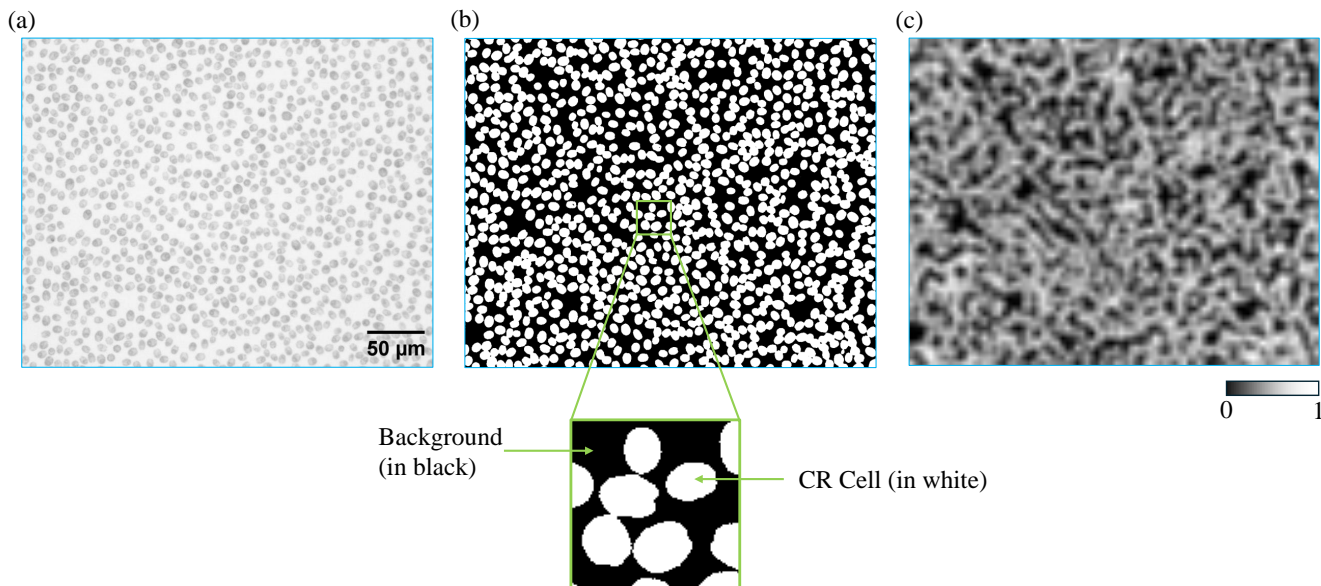


FIG. 3. (a) Optical image of a cell suspension. (b) Binarized image where the cells are shown in white and the background in black. (c) A gray-scale plot of the density obtained from the binary image.

video is captured with a Phantom Miro C110 Camera using a 20x bright field objective in an Olympus IX83 microscope.

- V3: This experimental video shows the spatiotemporal evolution of mbo2 cell suspensions with $\bar{\rho} = 0.51$. The video is captured with a Phantom Miro C110 Camera using a 20x bright field objective in an Olympus IX83 microscope.
- V4: This experimental video shows the spatiotemporal evolution of mbo2 cell suspensions with $\bar{\rho} = 0.71$. The video is captured with a Phantom Miro C110 Camera using a 20x bright field objective in an Olympus IX83 microscope.
- V5: This video shows the spatiotemporal evolution of the pseudocolor plots of the density field (left) and the vorticity ω [colour-bar unit sec^{-1}] field (right) for the WT cells (blue panel, $\bar{\rho} = 0.49$) and the mbo2 mutant (beige panel, $\bar{\rho} = 0.51$).